Accumulated CA–CFAR Process in 2-D for Online Object Detection From Sidescan Sonar Data

Gerardo G. Acosta, *Senior Member, IEEE*, and Sebastián A. Villar, *Member, IEEE*

***Abstract*—This paper describes a novel approach to object detection from sidescan sonar (SSS) acoustical images. The current techniques of acoustical images processing consume a great deal of time and computational resources with many parameters to tune in order to obtain good quality images. This is due to the handling of the large data volume generated by these kinds of devices. The technique proposed in this work does not make any *a priori* assumption about the nature of the SSS image to be processed. However, it is able to make a segmentation of the image into two types of regions: acoustical highlight and seafloor reverberation areas, and based on this, it makes detection. The developed algorithm to achieve this consists of a migration and adaptation of a technique widely used in radar technology for detecting moving objects. This radar technique is known as the cell average–constant false alarm rate (CA–CFAR). This paper presents a drastic improvement of such approach by making an extension into 2-D analysis of the SSS image, in a way similar to integral image used in CA–CFAR detection for pulse Doppler radar. In this form, optimization of the computational effort is achieved. This new technique was called the accumulated cell average–constant false alarm rate in 2-D (ACA–CFAR 2-D). It was applied to pipeline detection and tracking with a very interesting degree of success. In addition, this technique provides similar results to image segmentation with respect to other frequently used approaches, but with much less computational resources and parameters to set. Its simplicity is a strong support of its robustness and accuracy. This feature makes it particularly attractive for using it in real-time applications, such as underwater robotics perception systems. This proposal was tested experimentally with acoustical data from SSS and the results detecting pipelines, and other shapes like sunken vessels or airplanes, are presented in this paper. Likewise, an experimental comparison with the results obtained with inverse undecimated discrete wavelet transform (UDWT) and active contours techniques is also presented.**

***Index Terms*—Cell average–constant false alarm rate (CA–CFAR), online object detection, sidescan sonar (SSS), sonar imagery.**

Manuscript received November 01, 2013; revised July 21, 2014; accepted August 29, 2014. Date of publication October 20, 2014; date of current version July 10, 2015. This work was supported by MINECO from Spain under Grant DPI2009-11298, by CONICET under Grant PIP 11420090100238, and by MINCTIP from Argentina under Grant PICT-2009-0142.

Associate Editor: T. Maki.

G. G. Acosta is with the Grupo INTELYMEC, Centro de Investigaciones en Física e Ingeniería del Centro (CIFICEN), Consejo Nacional de Investigaciones Científicas y Técnicas (CONICET), Universidad Nacional del Centro de la Provincia de Buenos Aires (UNCPBA), Olavarría B7400JWI, Argentina and also with the Grup d'Enginyeria Electrònica (GEE), Departament de Física, Universitat de les Illes Balears, Palma, Spain (e-mail: gerardo.acosta@ieee.org).

S. A. Villar is with the INTELYMEC Group, Universidad Nacional del Centro de la Provincia de Buenos Aires (UNCPBA), Olavarría B7400JWI, Argentina (e-mail: svillar@fio.unicen.edu.ar).

Digital Object Identifier 10.1109/JOE.2014.2356951

I. Introduction

SONAR systems provide near-photographic high-resolution images of underwater areas, even in water with poor optical transparency [1]. The use of these acoustical images is important for many practical applications, such as marine geology, commercial fishing, resources search, extraction and oil drilling, inspection and maintenance of pipelines, mine detection, and waste or other targets monitoring [2]–[18].

Sidescan sonar (SSS) is an effective tool for high-resolution mapping of the seabed due to the maturity of the technology and, hence, the excellent cost/quality tradeoff [7]. It has been proved to work well in deep water [6], [8], [9], [12], [13]. Even though synthetic aperture sonar (SAS) systems provide higher quality imagery than conventional SSS systems using comparable operating frequencies, and have been used in numerous applications [16], [19]–[21], it is not yet clear that they are better for automated target detection and recognition purposes. Reports about the use of multibeam echosounders (MBEs) to explore seafloor in detail are also given in [6], [10], [22], and [23].

SSS uses linear arrays of transducers on the port and starboard sides, emitting and receiving in phase with one another, or in a controlled phase relationship. In each data acquisition cycle, the port and starboard beams extend sideways and downward, constituting a plane which advances in the direction of the speed vector of the vehicle transporting the SSS, named the along-track direction. The transducers on both sides of the sonar send oblique acoustical signals, in the shape of a fan. The direction that is perpendicular to the vehicle's straight movement is called the across-track direction. The acoustic frequencies are normally between 100 kHz and 1 MHz for shallow-water surveys. The port (left) and starboard (right) sides of the images are scanned separately. The acoustic pulses travel through the water column, hit the seafloor, and the echo or backscatter is returned to the reception sensor where its amplitude is quantified. This amplitude depends on the angle of incidence and the cover of the seafloor. The echoes coming directly from the seafloor constitute the true returned signal. There are also multiple bounces off the seafloor or the sea surface that constitute the reverberation or undesired echoes (multipath). The nadir and zenith correspond to points of low and high reflection off the surface of the seafloor and the surface of the sea, respectively. The data acquired are projected on a line traced along the seafloor. This scanning line is known as a swath. The acoustic data associated with this exploration line represent an observation of the reflected intensity depending on the range and the angle. If the

vehicle is moving in a straight line at a steady speed, the deployment of successive swaths will build an acoustical image of the seafloor in 2-D [24].

Usually, in the high-resolution images, SSS can identify three types of regions: acoustical highlight, shadow, and seafloor reverberation [25]. The highlight area originates from acoustical wave reflection from an object, whereas the shadow zone is due to a lack of acoustical reverberation behind the object. The remaining areas consist of the seafloor reverberation [4], [26].

As presented in [27], and suggested in [28], to achieve an object detection from an image, independently of the device employed, whether it be a sonar or a webcam, it is necessary to carry out a previous chain of processing to the image under analysis. One of these previous processing steps is segmentation, and it constitutes a bottleneck in the computational effort. When focusing on acoustical images, segmentation is based on the assumption that objects which are on the seafloor are usually more reflective than the surrounding sediment. For this reason, one of the segmentation alternatives is based on finding the maximum intensities of the backscattering, also called acoustical highlight. This acoustical highlight considerably varies according to the relative sonar orientation with regards to the target. In fact, it can fall below the detection threshold causing the target to appear invisible to the sonar [29]. In addition, an outstanding feature of SSS images is that the objects which stand out above the seafloor generate shadows. The shadow length depends on the vertical height of the object. Thus, the segmentation of these shadows can be used to achieve a detection, as proposed in [30]. Because the data acquisition is done from a moving vehicle, the sonar geometry with regard to the target is variable. Therefore, a shadow can be present even when the acoustical highlight is not. Thus, it would be desirable to combine both the acoustical highlight and the shadow detections. This approach was implemented in this work.

The seafloor reverberation region is more difficult to segment as it contains a large amount of speckle noise [1], typically present in all imaging systems with coherent illumination. The speckle noise renders ineffective the simple segmentation schemes of the digital image processing theory. For this reason, the simple implementation of such techniques turns out to be useless in the sonar imagery domain [28], [31]. To address these problems, it is important to incorporate contextual information [4], [26].

Conventional SSSs provide lines of acoustic returns that vary from 200 to 2000 samples. Note also that a greater quantity of samples implies more computational effort. The ability to segment high-resolution acoustic images efficiently is crucial for any practical application where detections and even pattern recognition are needed in an efficient time. One of such applications is the perception system of an autonomous underwater vehicle (AUV).

II. Previous Work

Many segmentation algorithm approaches for processing acoustical images are currently available. They vary in speed, efficiency (accuracy and robustness), sophistication degree, and required computational resources. These algorithms may be categorized as either supervised or unsupervised. Supervised seabed segmentation algorithms use a trained classifier with an assumption that there exists a finite set of segmented regions to be selected [9], [21], [32]–[34].

The unsupervised methods perform seabed segmentation by direct analysis of the input image without any *a priori* information. Among these approaches are multifractal analysis [33], Markov random field (MRF) model and hierarchical MRF (HMRF) [4], [26], local Fourier histograms (LFHs) [35], active contours [24], [36], Gauss–Markov random field model [25], and many others. Thus, all the aforementioned unsupervised seabed segmentation algorithms require either a learning stage to automate their process or computationally expensive mathematical models to segment into a predefined number of regions.

A recent technique that eliminates these problems is based on an algorithm that uses undecimated discrete wavelet transform (UDWT) [37]. It was used for acoustic processing in [1]. UDWT is exploited instead of the discrete wavelet transform because of its following characteristics: 1) there is no downsampling and thus there is no aliasing problem; and 2) it is shift invariant, i.e., the decomposition of image between levels of a multiscale decomposition does not vary if the original image is shifted before decomposition. The authors proposed a feature vector for each pixel constructed by sampling the intraresolution and interresolution data to create a feature vector field for the overall input image. The final segmentation is achieved by clustering the feature vector field into disjoint classes using k-means.

This paper proposes an algorithm that requires neither a prior learning process nor computationally expensive mathematical models to make object detection, and implicitly, image segmentation. A group of target detection techniques widely used in the radar [38] technology is known as constant false alarm rate (CFAR), thoroughly described in [39]. This group of techniques maintains a CFAR computed from the last n samples of the digitalized echo power. The echo power is also known as interference power. In this way, an adaptive detection threshold is adjusted to maintain a probability of expected false alarm (P_{fa}) by estimating the average of the interference power values of the adjacent n cells. As a result of this processing technique, detections are enriched with contextual information. This approximation is called the cell averaging–constant false alarm rate (CA–CFAR) [39].

CA–CFAR is then an adaptive technique which estimates the detection threshold based on the interference power in the surroundings of the test cell. Note also that, considering this contextual information, both the acoustic highlight and the shadow that the targets generate are taken into account to make a detection. The technique assigns strong return values proportional to the area of the present target, and weak values proportional to the shadow area behind it. These abrupt variations facilitate the detection task. These concepts were successfully used in the implementation of the CA–CFAR algorithm for pulsed-Doppler radar [44]. The work of Venter *et al.* inspired the shift of the ideas from radar to sonar, interpreting the interference power in radar as the acoustic reverberation power in sonar. Even further, the integral image approach [45] used there to speed up computations was also adapted and improved for sonar images, as will be shown in Sections IV and V.

The objectives explored in this paper are focused on segmenting two types of regions: acoustic highlight and seabed reverberation areas. In addition, the purpose of this work is to optimize computing resources without losing robustness. Hence, the proposed algorithm represents a 2-D extension of accumulated cell averaging–constant false alarm rate (ACA–CFAR) [27]. The ACA–CFAR 2-D is then another variant for standard CA–CFAR in 2-D. From this segmentation, pipeline detection is achieved successfully and efficiently in terms of computational effort and robustness, as presented in next paragraphs. In addition, it will be demonstrated that ACA–CFAR 2-D can be used as a segmentation algorithm with similar performances to UDWT [1] and active contour [24] techniques for the same acoustic images, but giving better results in central processing unit (CPU) resources and executing times.

This paper is organized as follows. Section II shows the basic concepts of the detection theory with CA–CFAR. Section III presents the method of ACA–CFAR 2-D. In Section IV, the experimental results, analyses, and comparisons are given. Finally, Section V discusses the conclusions and new perspectives obtained from this work.

III. Object Detection Using CA–CFAR

The problem of detection consists of analyzing the acoustical intensity in each sample with the purpose of detecting the presence or absence of a target. Detection techniques are generally implemented by analyzing the information of adjacent samples. In [39], there are two hypotheses defined for this analysis: 1) the sample is the background (H_0); and 2) the sample is a combination of a background and a target (H_1). Consequently, the detection consists in examining each sample and selecting one of these hypotheses as the best. If hypothesis H_0 is more appropriate, the detection system declares that the target is not present. If hypothesis H_1 is more appropriate, the detection system declares that the target is present. Because the signals are described statistically, the decision between these two hypotheses represents an exercise of statistical decision theory [40].

Fig. 1 shows a generic architecture of the CA–CFAR process [41] applied on a row vector of $(1 \times n)$ samples. Each sample of acoustic intensity is associated with a test cell (x_i). Each cell represents one pixel, referring to a spatial coordinate (x, y) of the image. A detection threshold (T) is estimated based on the surroundings of this test cell and a multiplier (α). This multiplier is a constant that is determined based on the false alarm probability (P_{fa}) to attenuate or amplify the detection threshold. Hence, the CA–CFAR technique maintains constant false alarm rate (P_{fa}) but a varying detection threshold. This means that contextual information is taken into account in the determination of the detection threshold. This turns CA–CFAR into an adaptive technique to make detections based on contextual information. Then, the current test cell (x_i) is compared to the detection threshold (T). If the test cell value exceeds the threshold, the process declares that the target is present. The process is applied to the next cell in a recursive way. The technique assigns strong return values when the acoustical highlight is proportional to the area of the target frontal part, and weak values when it is proportional to the length of the shadow behind the object. These abrupt variations between a highlight range and acoustic shadow generate the target detection possibility.

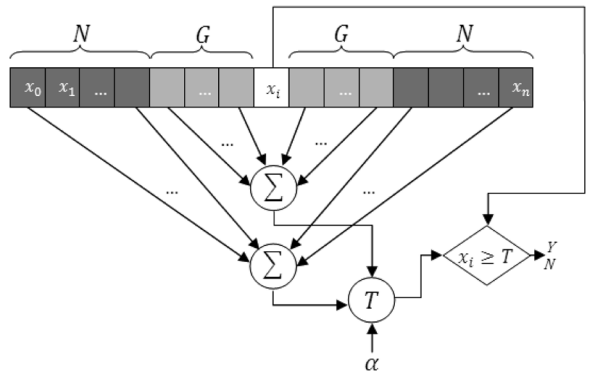

Fig. 1. Generic architecture of the CA–CFAR process [41].

In Fig. 1, a row vector of $(1 \times n)$ cells is depicted. Both dark gray as well as light gray cells represent the neighboring data that will be averaged to estimate the detection threshold. The dark gray cells are called reference cells (N). The lighter gray cells, immediately next to the test cell (x_i), are called guard cells (G). These cells are excluded from the average because if the target is present, then the neighbor cells will contain similar high values of backscattering. The increase in acoustic highlight due to the presence of the target should tend to increase the probability of exceeding the threshold and thus generate detection.

The total number of neighbor cells (N_c) around the test cell is calculated utilizing[1]

$$N_c = 2N + 2G + 1. \tag{1}$$

In the same way, the number of guard cells (G_c) is computed utilizing

$$G_c = 2G + 1 \tag{2}$$

with $G < N$ (see Fig. 1).

The procedure to determine the detection threshold (T) is described below. Let us consider the case of a Gaussian reverberation, as is done in radar technology, with a square law detector. The probability density function (pdf) for any cell $x_i \geq 0$ has only one free parameter, which is the mean of the acoustic reverberation power (β^2). For the purpose of this work, and as is validated in the experiments, the concept of interference power introduced in [39] and used in [44] is considered here as the acoustic reverberation power. Likewise, the process estimates the mean of the reverberation power in the test cell (x_i) using the adjacent cells data, with

$$f_{\bar{x}_i}(x_i) = \frac{1}{\beta^2} e^{-x_i/\beta^2}, \qquad \text{with } x_i \geq 0. \tag{3}$$

The distribution in (3) is assumed from the proposal for radar detection in [39], from where the CFAR methodology was borrowed. Note that this is a strong working hypothesis that should be validated with experimental results. As will be

[1]The presence "+1" in (1) and (2) is only, due to computational reasons, to take into consideration also the test cell.

shown in Section IV, this hypothesis worked well in the cases study. However, many other probability distributions should be tested in the future.

It is supposed that the content of (N_c) cells, which are neighbors to the cell under test (x_i), will be used to estimate the acoustic reverberation power (β^2). Another supposition is that reverberations are independent and identically distributed (i.i.d.). Then, the joint pdf $f_{\bar{x}_i}$ for a vector $\bar{x}_i = (x_1, x_2, \ldots, x_{N_c})$ of neighboring cells (N_c) is

$$f_{\bar{x}_\mathrm{i}}(x_1, x_2, \ldots, x_{N_c}) = \prod_{i=1}^{N_c} f_{x_i}(x_i).$$

Using (3)

$$\begin{aligned} f_{\bar{x}_\mathrm{i}}(x_1, x_2, \ldots, x_{N_c}) &= \prod_{i=1}^{N_c} \frac{1}{\beta^2} \cdot e^{-x_i/\beta^2} \\ &= \frac{1}{\beta^{2N_c}} \cdot e^{-\frac{1}{\beta^2}\left(\sum_{i=1}^{N_c} x_i\right)}. \end{aligned} \tag{4}$$

Equation (4) is the likelihood function $\wedge$ for the vector of observed data $\bar{x}$. The maximum estimated likelihood (m.e.l.) of the acoustic reverberation power is obtained by maximizing (4) with respect to (β^2) [40]. Mathematically, it is equivalent, and generally easier to maximize, the log-likelihood function [39]

$$\ln \bigwedge = -N_c \ln(\beta^2) - \left(\frac{1}{\beta^2}\right)\left(\sum_{i=1}^{N_c} x_i\right). \tag{5}$$

Differentiating (5) with respect to (β^2) and equating it to 0 yields

$$\widehat{\beta^2} = \frac{1}{N_c}\sum_{i=1}^{N_c} x_i. \tag{6}$$

The detection threshold $(\hat{T})$ required is estimated as a scalar multiple $\alpha > 0$ of reverberation power

$$\hat{T} = \alpha\widehat{\beta^2}. \tag{7}$$

This adaptive threshold allows considering a constant false alarm probability, even when the reverberation levels vary. The threshold $(\hat{T})$ computed by (7) is a random variable. The detector is considered as a CFAR one, if the value of the probability of false alarm (P_{fa}) does not depend on the current value of (β^2). Combining (6) and (7) yields the expression for the estimated threshold

$$\hat{T} = \frac{\alpha}{N_c}\sum_{i=1}^{N_c} x_i. \tag{8}$$

Defining $z_i = (\alpha/N_c)x_i$, such that $\hat{T} = \sum_{i=1}^{N_c} z_i$, and using the standard result of the probability theory with (3) yields the pdf of z_i

$$p_{z_i}(z_i) = \frac{N_c}{\alpha\beta^2} e^{-\frac{N_c z_i}{\alpha\beta^2}}, \qquad \text{with } z_i \geq 0. \tag{9}$$

This pdf of $(\hat{T})$ given by (9) is known as the Erlang density [42] with parameters N_c and $N_c/\alpha\beta^2$

$$p_{\hat{T}}(\hat{T}) = \left(\frac{N_c}{\alpha\beta^2}\right)^{N_c} \frac{\hat{T}^{N_c-1}}{(N_c-1)!} e^{-N_c\hat{T}/\alpha\beta^2}. \tag{10}$$

The observed (P_{fa}) was computed [40] from the estimated threshold as $\exp(-\hat{T}/\beta^2$, which is also a random variable. Then, its expected value was computed as

$$\begin{aligned} \bar{P}_{fa} &= \int_0^\infty e^{-\frac{\hat{T}}{\beta^2}} p_{\hat{T}}(\hat{T}) d\hat{T} \\ \bar{P}_{fa} &= \left(\frac{N_c}{\alpha\beta^2}\right)^{N_c} \frac{1}{(N_c-1)!} \int_0^\infty \hat{T}^{N_c-1} e^{-\left|\left(\frac{N_c}{\alpha}\right)+1\right|\hat{T}/\beta^2} d\hat{T}. \end{aligned} \tag{11}$$

Completing this standard integral and carrying out some algebraic manipulation, the final result was obtained

$$\bar{P}_{fa} = \left(1 + \frac{\alpha}{N_c}\right)^{-N_c}. \tag{12}$$

For an expected $(\bar{P}_{fa})$, the required value of the multiplier (α) is acquired from solving (12)

$$\alpha = N_c\left(\bar{P}_{fa}^{-\frac{1}{N_c}} - 1\right). \tag{13}$$

Note that $(\bar{P}_{fa})$ does not depend on the acoustic reverberation power (β^2), but on the number (N_c) of neighboring cells. Thus, the technique of cell average exhibits the CFAR behavior. Only P_{fa}, N, and G must be determined beforehand. As will be demonstrated experimentally in Sections IV and V, a drastic reduction of computation times and high robustness due to the selection of few parameters can be obtained with this approach.

IV. ACA–CFAR 2-D

As reported in [43], it was possible to achieve pipeline detection from acoustic images of an SSS with the standard CA–CFAR methodology. In addition, a variation of this approach, partial sums CA–CFAR, was introduced and tested experimentally. In turn, in [27], we also showed a variation in implementation called ACA–CFAR 1-D that provided similar results but with improved computational time and resources over CA–CFAR. The ACA–CFAR 2-D presented in this paper represents a further improvement to the implementation of the standard CA–CFAR described in Section III, extended to 2-D. Fig. 2 shows graphically generic windows for 1-D and 2-D. In this new situation, the detection threshold $(\hat{T})$ computation, with (6) and (7), is carried out using a sliding window with reference and guard cells in 2-D, as depicted in Fig. 2, in a similar way as the integral image presented in [44] and [45].

Estimating the threshold for each cell (x_{ij}) requires $N_c = [2(N+G)+1]^2$ memory accesses to calculate the sum of the reference cells, and $G_c = (2G+1)^2$ new memory accesses for the guard cell computations.

This estimate requires excessive computational resources and time to analyze an entire acoustic image, typically in the range of 200–2000 samples. For this reason, the main contributions of this work are: 1) to improve the computational effort by previous calculation of the summations of the reference cells and guard; and 2) to simplify the required parameters to be set in a normal detection.

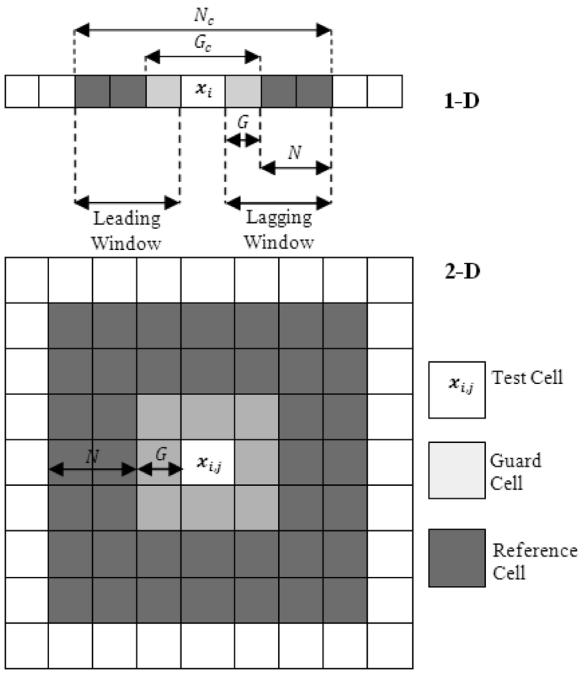

Fig. 2. Generic CFAR windows for 1-D and 2-D [39]. Both window options 1-D and 2-D contain $N = 2$ and $G = 1$. The total numbers of reference and guard cells are $N_c = 7$ and $G_c = 3$, respectively, for 1-D and $N_c = 49$ and $G_c = 9$, respectively, for 2-D.

Acoustic Data Samples

	1	2	3	4	5	6
1	x_{11}	x_{12}	x_{13}	x_{14}	x_{15}	x_{16}
2	x_{21}	x_{22}	x_{23}	x_{24}	x_{25}	x_{26}
3	x_{31}	x_{32}	x_{33}	x_{34}	x_{35}	x_{36}
4	x_{41}	x_{42}	x_{43}	x_{44}	x_{45}	x_{46}
5	x_{51}	x_{52}	x_{53}	x_{54}	x_{55}	x_{56}
6	x_{61}	x_{62}	x_{63}	x_{64}	x_{65}	x_{66}

Accumulated Samples Matrix

	0	1	2	3	4	5
0	Acc_{11}	Acc_{12}	Acc_{13}	Acc_{14}	Acc_{15}	Acc_{16}
1	Acc_{21}	Acc_{22}	Acc_{23}	Acc_{24}	Acc_{25}	Acc_{21}
2	Acc_{31}	Acc_{32}	Acc_{33}	Acc_{34}	Acc_{35}	Acc_{31}
3	Acc_{41}	Acc_{42}	Acc_{43}	Acc_{44}	Acc_{45}	Acc_{41}
4	Acc_{51}	Acc_{52}	Acc_{53}	Acc_{54}	Acc_{55}	Acc_{51}
5	Acc_{61}	Acc_{62}	Acc_{63}	Acc_{64}	Acc_{65}	Acc_{66}

Fig. 3. Example of the distribution of acoustical data samples and accumulated sample matrix using (16) for ACA–CFAR 2-D.

Fig. 3 shows an example of the samples distribution x_{ij} (with $i = 1, \ldots, r$ and $j = 1, \ldots, c$ where r and $c$represent the size of rows and columns of the image, respectively). Suppose there is a selection of reference cells $N = 2$ and a guard cell $G = 1$. It is convenient to define a distance from the test cell to the farthest cell in the guard window, called guard distance $d_g = G$. In the same way, reference distance $d_r = N + G$ is defined as the one between the test cell and the farthest cell in the reference window. Thus, the total number of reference cells to estimate the power of acoustical reverberation can be calculated with

$$N_c = (2.d_r + 1)^2 \tag{14}$$

and the total number of guard cells can be calculated with

$$G_c = (2.d_g + 1)^2. \tag{15}$$

For this example

$$N_c = (2.d_r + 1)^2 = (2.3 + 1)^2 = 49$$
$$G_c = (2.d_g + 1)^2 = 9.$$

The ACA–CFAR 2-D technique computes an accumulated absolute samples vector Acc_{rc} beforehand, for each cell, using

$$\mathrm{Acc}_{rc} = \sum_{i=1}^{r} \sum_{j=1}^{c} x_{ij}. \tag{16}$$

Refer to Fig. 3.

Thus, the double summation $\sum_{rc}$ in rows and columns is now used to calculate the threshold, as an extended 2-D version of (8). In this way, this double summation is calculated using only the algebraic sum of four terms of the matrix elements computed beforehand by means of (16) yielding

$$\sum_{rc} = \mathrm{Acc}_{d_r+r,d_r+c} - \mathrm{Acc}_{r-d_r-1,d_r+c} - \mathrm{Acc}_{d_r+r,c-d_r-1} + \mathrm{Acc}_{r-d_r-1,c-d_r-1}. \tag{17}$$

In other words, we want to make a fast computation of the sum $\sum_{rc}$ with pixels in a square $(2.d_r+1)^2$ from pixel (r, c) by using beforehand accumulated absolute sample vectors Acc_{rc}, because it requires only four memory accesses.

The four terms in (17) represent the vertices of the window sliding on the accumulated matrix. The first term $(\mathrm{Acc}_{dr+r,dr+c})$ is the lower right corner, which represents the accumulated total. The second term $(\mathrm{Acc}_{r-d_r-1,d_r+c})$ is the lower left corner, which refers to the accumulated column in position (r, c) to be subtracted from the accumulated total. The third term $(\mathrm{Acc}_{d_r+r,c-d_r-1})$ corresponds to the upper right corner and refers to the cumulative row at position (r, c) also to be subtracted from the accumulated total. Finally, the fourth term $(\mathrm{Acc}_{r-d_r-1,c-d_r-1})$ is the upper left corner that must be added to the accumulated total because both second and third terms were subtracted two times and must be subtracted only once.

For the guard cell computations, the procedure is similar, just changing d_r by d_g in (17) and obtaining

$$\sum_{rc} = \mathrm{Acc}_{d_g+r,d_g+c} - \mathrm{Acc}_{r-d_g-1,d_g+c} - \mathrm{Acc}_{d_g+r,c-d_g-1} + \mathrm{Acc}_{r-d_g-1,c-d_g-1}. \tag{18}$$

Note that this is valid for the general case in which samples are away from the edges of the image, in other words, the distance $d \geq d_r$ for left, right, above, or below on the test cell. Otherwise, there are the following special cases. In these special cases, N_c decreases as the test cell approaches the edges of the image.

Case 1) If $r - d_r - 1 \leq 0$ and $c - d_r - 1 \leq 0$, there is only one valid term in the general equation because the other terms are outside the boundaries of the image

$$\sum_{rc} = \mathrm{Acc}_{d_r+r,d_r+c}. \tag{19}$$

Case 2) If $r - d_r - 1 \leq 0$, there are only two valid terms in the general equation because the other terms are outside the boundaries of the image. The second term of

$$\sum_{rc} = \mathrm{Acc}_{d_r+r,d_r+c} - \mathrm{Acc}_{d_r+r,c-d_r-1} \tag{20}$$

represents the subtraction of an accumulated column, which is outside the boundaries of the reference window.

Case 3) If $c - d_r - 1 \leq 0$, there are only two valid terms in the general equation because the other terms are outside the boundaries of the image. The second term of

$$\sum_{rc} = \mathrm{Acc}_{d_r+r,d_r+c} - \mathrm{Acc}_{r-d_r-1,d_r+c} \tag{21}$$

represents the subtraction of an accumulated row, which is outside the boundaries of the reference window.

Analyzing this ACA–CFAR 2-D technique, it appears that once the accumulated samples matrix is computed, with only four memory accesses as an upper bound, the average of the acoustic interference surrounding the cell can be calculated. Similarly, with four additional memory accesses, the guard cell averaging can be obtained. Note that the standard technique in 2-D would have required N_c and G_c memory accesses for the same calculation for any test cell. As will be shown quantitatively in Section V, we obtained a much more efficient algorithm in this way. With this approach, even in the case that N_c and G_c are increased, the upper bound of four memory accesses will be maintained as constant, improving the computational effort in calculating the threshold.

When computing and depicting the threshold's surface for an image, some questions arise. Is it necessary to look for a detection in regions of the image where there is only noise? How can one exclude these noisy regions beforehand to reduce the computing effort? Can we take advantage of some of the calculations done when applying the ACA–CFAR 2-D technique? Fortunately, it seems that there are some possible ways to improve the detection process applying the answers to these questions. In the present approach, one can resort to the accumulated samples matrix, in the last position $(\mathrm{Acc}_{n,m})$, where there is computed accumulated summation of the acoustic intensity of all of the image's pixels. Then, dividing it by the total number of cells (*nxm*), an average lower boundary B_l can be computed. Only if the sample x_{ij} is greater than the threshold $\bar{T}_{ij}$ and $\bar{T}_{ij}$ is greater than B_l, then a detection is confirmed. This slight variation in the algorithm causes a drastic enhancement of the ACA–CFAR 2-D technique. Effectively, it allows focusing its application only in those regions of the image where there are targets of interest to be detected, without applying it to regions with only noise.

Pseudocode: ACA–CFAR 2–D

Variables: *image, acc, pfa, alpha, N, G, nc, sumN, sumG, threshold, lowerBoundary, labelHighlight, labelBackground*

image: acoustic image; *acc*: accumulated samples by rows and columns; *pfa*: false alarm probability; *alpha*: alpha multiplier; *N*: number of reference cells; *G*: number of guard cells; *nc*: number of cells for each estimate; *sumN*: sum of reference cells; *sumG*: sum of guard cells; *threshold*: detection threshold; *lowerBoundary*: lower limit for detection; *labelHighlight*: acoustic highlight label; *labelBackground*: seabed reberveration label.

Method:

BEGIN
FOR (row ← 0 **to** row < HEIGHT **increase** +1)
FOR (col ← 0 **to** col < WIDTH **increase** +1)
IF (row == 0 **AND** col == 0**) THEN**
acc [row, col] ← *image* [row, col]
ELSE IF (row == 0**) THEN**
acc [row, col] ← *acc* [row, col–1] + *image* [row, col]
ELSE IF (col == 0**) THEN**
acc [row, col] ← *acc* [row–1, col] + *image* [row, col]
ELSE
acc [row, col] ← (*acc* [row, col–1] – *acc* [row–1, col–1])
+ *acc* [row–1, col] + *image* [row, col]
lowerBoundary ← *acc* [HEIGHT-1, WIDTH-1]/
(HEIGHTxWIDTH)
FOR (row ← 0 **to** row < HEIGHT **increase** +1)
FOR (col ← 0 **to** col < WIDTH **increase** +1)
nc ← ***calculateSamples*** (row, col, *N*+*G*)
alpha ← $nc * (pfa^{-1/nc} - 1)$
sumN ← ***calculateSumCells*** (*acc*, row, col, *N*+*G*)
sumG ← ***calculateSumCells*** (*acc*, row, col, *G*)
threshold ←((*sumN* – *sumG*) / *nc*) * *alpha*
value ← *image* [row, col]
IF (*value>threshold* **AND** *threshold>lowerBoundary***)**
THEN
image [row, col] ← *labelHighlight*
ELSE
image [row, col] ← *labelBackground*
END

Fig. 4. Pseudocode of the ACA–CFAR 2-D technique.

Fig. 4 shows in detail the pseudocode of the ACA–CFAR 2-D technique. As can be seen, there are two well-defined portions of the code. The first group of statements calculates the accumulated samples by rows and columns (*acc*) used for estimating the summations of reference and guard cells with (16). The second group of statements is separated into acoustical highlights (*labelHighlight*) and seafloor reverberation (*labelBackground*) areas.

For each sample of the acoustical image (*image*) the detection threshold (*threshold*) is estimated with the 2-D version of (7). To do this, one must calculate the number of samples in each estimate (*nc*), the multiplier alpha (α) establishing a constant probability of false alarm (P_{fa}) with (13), the sum of reference (*SumN*), and guard (*SumG*) cells. The number of samples (*nc*) uses a function called *calculateSamples*, which depends on the current position in the image (*row* and *col*) and the reference distance $(d_r = N + G)$. To calculate the sum of the reference (*SumN*) and guard (*SumG*) cells, a function called *calculateSumCells* is used, which depends on the accumulated samples matrix (*acc*), the current position in the image (*row* and *col*), and the reference $(d_r = N + G)$ and guard $(d_g = G)$ distances. As a final result, the segmentation into two regions is computed and stored in the same variable called *image*.

For the particular case of pipeline tracking, from the pixels labeled as detection, an additional computation regarding the turn radius among them is necessary to be done to ensure topological

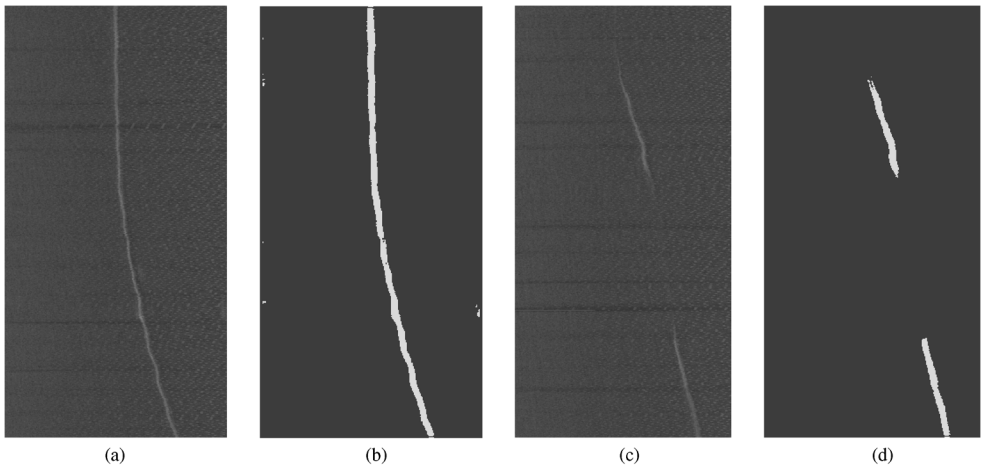

Fig. 5. Sonar image (Sonar Starfish 450F using a frequency of 450 kHz with a range of 50 m) of an oil pipeline located approximately 18 m deep: (a) input sonar image of curved pipe; (b) detected pipeline of (a) using ACA–CFAR 2-D; (c) input sonar image of a pipeline partially buried; (d) detected pipeline of (c) using ACA–CFAR 2-D.

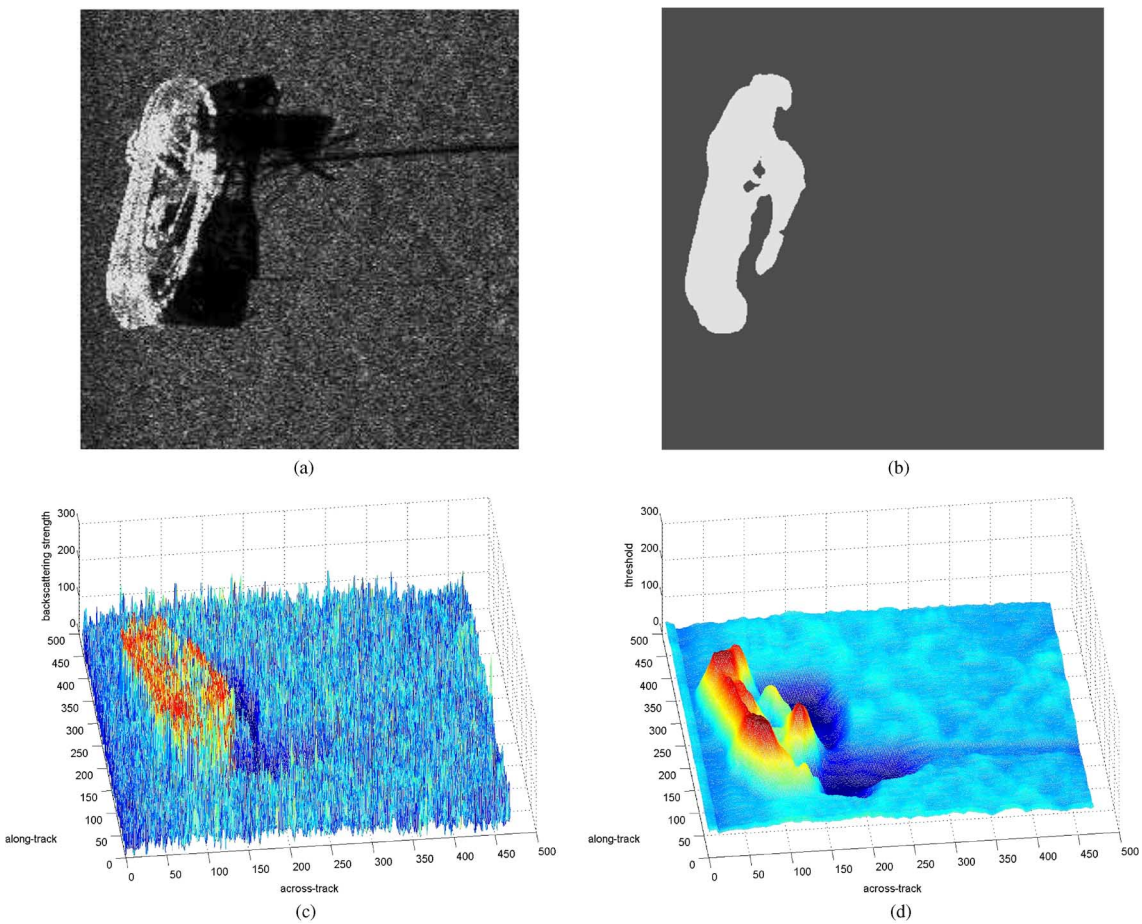

Fig. 6. Sonar image of a sunken ship: (a) input sonar image; (b) segmented image using ACA–CFAR 2-D; (c) input sonar image plotted in 3-D (across-track, along-track, and backscattering strength); and (d) detection threshold surface ($\hat{T}$) plotted in 3-D (across-track, along-track, and threshold).

continuity. This calculation involves very little computational effort [6].

V. Experimental Results and Comparisons

The algorithms were developed originally with MATLAB and then were ported to code written in C++, taking advantage of the data structure within OpenCV 2.3 [46]. The programming environment (IDE) was Nokia Qt Creator for GNU/Linux implementation code C ++. The algorithms were executed on a PC with a CPU 2-GHz Intel Core 2 Duo, and 2-GB RAM memory, with Linux OS. The experimental data employed in this work were acoustic images of an SSS of the seafloor.

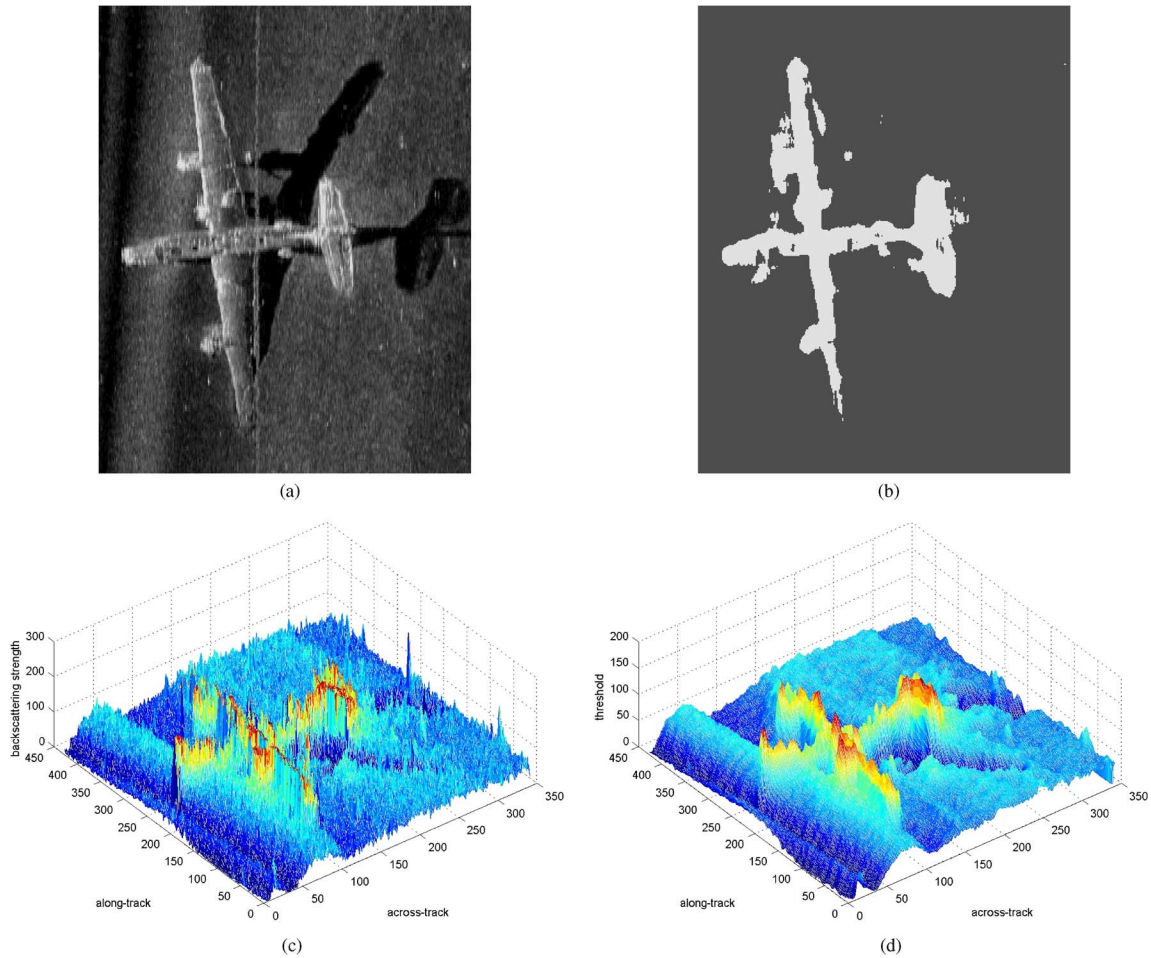

Fig. 7. Sonar image (600 kHz with a range of 50 m) of a sunken airplane (Consolidated PB4Y2 Privateer) in Lake Washington: (a) input sonar image; (b) segmented image using ACA–CFAR 2-D; (c) original image plotted in 3-D (across-track, along-track, and backscattering strength); and (d) detection threshold surface ($\hat{T}$) plotted in 3-D (across-track, along-track, and threshold).

TABLE I
RUNNING PARAMETERS OF ACA–CFAR 2-D AND SETTINGS FOR PIPELINE TRIALS

Fig.	N	G	N_c	G_c	P_{fa}	T	N° I
5(a)-(b)	2	1	49	9	0.35	0.077	124476
5(c)-(d)	2	1	49	9	0.35	0.082	122018

N: The number of reference cells. G: The number of guard cells. N_c: The total number of neighbor cells. G_c: The total number of guard cells. P_{fa}: False alarm probability. T: Runtime in seconds. N°I: The total number of instructions computed with (23).

The experiments consisted of the first approach to the problem domain, that is, the online pipeline detection. The efficient time detection was necessary as a previous step to include the ACA–CFAR 2-D algorithm into the perception system of an AUV. In addition, a second set of tests were done to contrast the segmentation power of ACA–CFAR 2-D against other commonly used segmentation techniques. To make the comparisons, a quantitative measure of image segmentation was needed, as explained in Section V-A. Even though the concept of segmentation is subjective and application dependent due to there being no single standard method of image segmentation [31], we decided to use the segmentation as described in [1] to facilitate the comparison.

A. Quantitative Measure of Image Segmentation

Two figures of merit were computed for comparisons with the technique described in [1]: 1) the proportion (ρ) of segmented images; and 2) runtime in seconds. The measure (ρ) is employed for comparing the segmentation map (SM) with the ground-truth segmentation map ($\mathrm{SM_{GT}}$) using

$$\rho = 1 - \frac{\sum_{i=1}^{S_w}\sum_{j=1}^{S_a} \varnothing\left(\mathrm{SM_{GT}}(i,j), \mathrm{SM}(i,j)\right)}{S_w S_a} \tag{22}$$

where S_w and S_a represent the number of swaths and the number of samples, respectively. Here, $\varnothing(a,b) = 1$ when $a = b$, and $\varnothing(a,b) = 0$ when $a \neq b$. When $\mathrm{SM_{GT}}$ and SM are the same, then ρ is 1, and ρ approaches 0, when the dissimilarity between $\mathrm{SM_{GT}}$ and SM increases.

The other figure of merit in [1] was the executing time, which is very dependent on hardware. For these experiments, the same hardware was used for all the testing. However, to set the basis for a more accurate and objective comparison, the number of instructions required to execute the algorithms is proposed. For ACA–CFAR 2-D, this figure of merit was computed with

$$\#\mathrm{I} = S_w \cdot S_a. \tag{23}$$

Note that the performance index of (23) is constant for the same image, depending only on the number of samples (S_a).

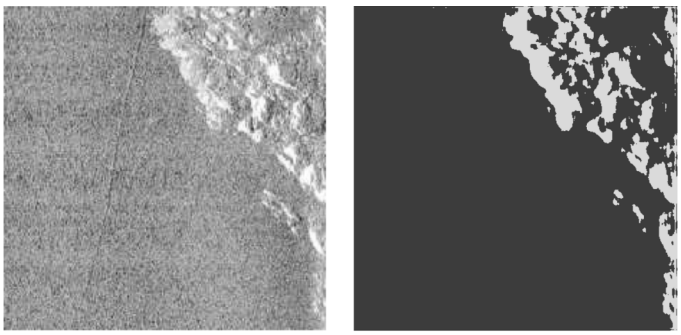

(a) (b)

Fig. 8. Sonar image of rocks on seafloor: (a) input sonar image; (b) segmented image using ACA–CFAR 2-D.

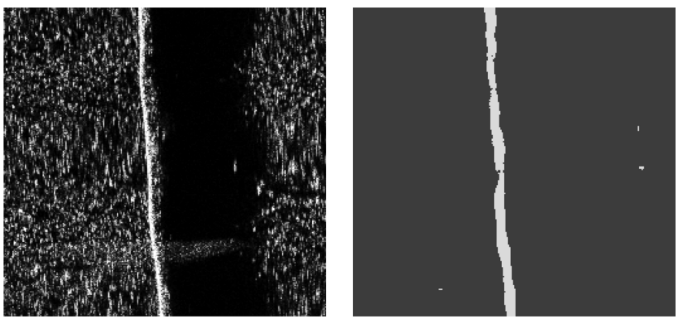

(a) (b)

Fig. 9. Sonar image of pipeline on seafloor: (a) input sonar image; (b) segmented image using ACA–CFAR 2-D.

Further, (23) gives the possibility to measure the algorithmic complexity, which is $O(S_w \cdot S_a)$. When the image is square, its complexity is of quadratic order $O(N^2)$ where N^2 is the number of cells to be analyzed.

B. Pipeline Detection

Fig. 5 shows an image of the seafloor of Salvador de Bahia, Brazil, where there is an exposed pipeline. For SSS detection, it is necessary that the pipeline be exposed fully or partially. When buried, the sensing system should have a magnetic tracker or a sub-bottom profiler, which was not the case in these sea trials. The pipeline tracking had two stages. The first one was initiated at latitude 12° 51′ 19.5″ S, and longitude 38° 32′ 23.03″ W and concluded at latitude 12° 52′ 23.28″ S and longitude 38° 33′ 48.48″ W. The system collected 50 500 lines of valid acoustical data, yielding 101 images of 1000 × 500 pixels for testing the algorithms. The second stage started at latitude 12° 53′ 33.04″ S and longitude 38° 33′ 48.14″ W and concluded at latitude 12° 52′ 16.1″ S and longitude 38° 31′ 37.14″ W, collecting 47 000 lines of acoustical data and totaling 94 images of the same size as the ones obtained for the first test stage. The SSS was a StarFish 450F, utilizing advanced digital CHIRP acoustical technology, and set at a frequency of 450 kHz with a range of 50 m.

Table I shows the parameter settings and performance results of ACA–CFAR 2-D to yield detections of Fig. 5. The P_{fa} was set constant for the whole image shown in each figure. The adaptation for detection was done through the threshold, as is mandatory in the CFAR techniques. Note that the algorithm has a window distortion effect [i.e., compare Fig. 5(a) and (c) with Fig. 5(b) and (d)]. This can be corrected with posterior image processing. However, for the aim of automated pipeline tracking, this was not necessary.

TABLE II
RUNNING PARAMETERS OF ACA–CFAR 2-D AND SETTINGS FOR SUNKEN SHIP AND AIRPLANE

Fig.	N	G	N_c	G_c	P_{fa}	T	N° I
6	10	2	625	25	0.36	0.126	220900
7	2	1	49	9	0.37	0.092	145948

N: The number of reference cells. G: The number of guard cells. N_c: The total number of neighbor cells. G_c: The total number of guard cells. P_{fa}: False alarm probability. T: Runtime in seconds. N°I: The total number of instructions computed with (23).

TABLE III
RUNNING PARAMETERS OF ACA–CFAR 2-D AND SETTINGS FOR DIFFICULT CASES

Fig.	N	G	N_c	G_c	P_{fa}	T	N° I
8	2	1	49	9	0.47	0.125	221841
9	4	0	81	1	0,2	0.052	65536

N: The number of reference cells. G: The number of guard cells. N_c: The total number of neighbor cells. G_c: The total number of guard cells. P_{fa}: False alarm probability. T: Runtime in seconds. N°I: The otal number of instructions computed with (23).

TABLE IV
PERFORMANCE AND RUNTIME RESULTS OF DIFFERENT APPROACHES

Fig.	Active Contours		UDWT		ACA-CFAR 2-D	
	ρ	T	ρ	T	ρ	T
10.1	97.7	309.18	98.64	2.15	82.08	0.142
10.2	87.52	288.92	92.94	2.33	80.50	0.148
10.3	84.69	322.78	92.80	2.22	85.57	0.15

Active contours [24]. UDWT [1]. ρ: Percentage of segmented images. T: Runtime in seconds.

TABLE V
RUNNING PARAMETERS OF ACA–CFAR 2-D AND SETTINGS FOR DIFFERENT SEGMENTATION APPROACHES COMPARISON

Fig.	N	G	N_c	G_c	P_{fa}	N° I
10.1	8	1	361	9	0.39	256036
10.2	6	2	289	25	0.39	256036
10.3	3	1	81	9	0.36	256036

N: The number of reference cells. G: The number of guard cells. N_c: The total number of neighbor cells. G_c: The total number of guard cells. P_{fa}: False alarm probability. N°I: The total number of instructions computed with (23).

C. Use of ACA–CFAR 2-D in Segmentation of Other Objects

A set of images was selected from available websites [47], [48] for this second phase of experiments. These images are shown in Figs. 6–10. Fig. 6 shows a sunken ship and Fig. 7 shows a sunken airplane in Lake Washington. These kinds of images have a special interest, for instance, in automated rescues searches and archeological studies. Fig. 6(b) presents the segmentation provided by ACA–CFAR 2-D, set with the parameters of Table II. Also, in this table, there are remaining settings of the whole experiment. Fig. 6(c) shows a virtualization of the input image from sonar, and Fig. 6(d) shows a

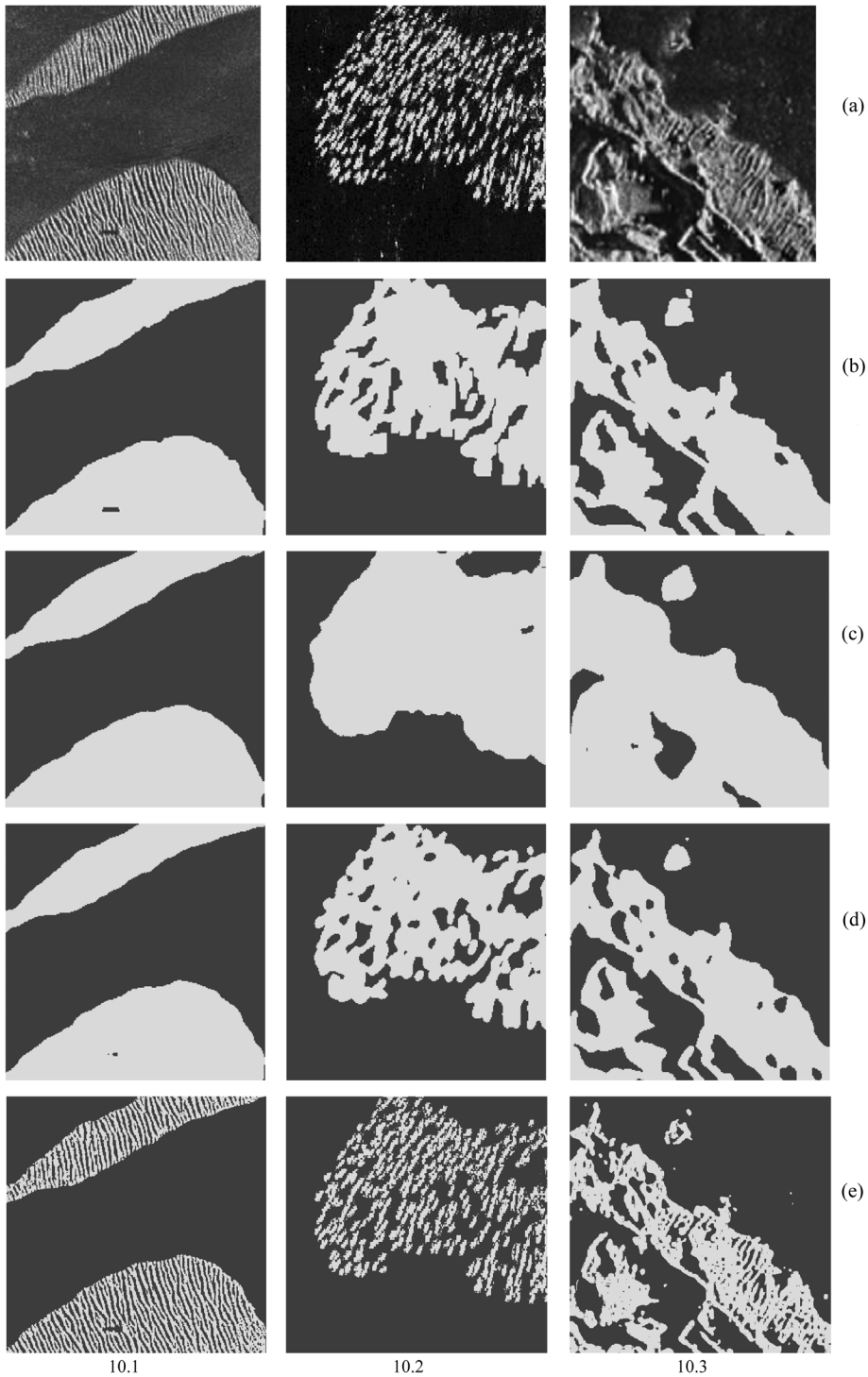

Fig. 10. Seabed segmentation using different algorithms: (a) input sonar images; (b) ground-truth segmentation maps; and segmentation results using: (c) active contours [24], (d) UDWT [1] and (e) the proposed algorithm (ACA–CFAR 2-D).

3-D representation of the threshold surface computed by the ACA–CFAR 2-D running. Similarly, Fig. 7(b) presents the segmentation of the image in Fig. 7(a) provided by ACA–CFAR 2-D, set with the parameters of Table II. Fig. 7(c) shows a virtualization of the input image from sonar, and Fig. 7(d) shows a 3-D representation of the threshold surface computed by the ACA–CFAR 2-D technique.

A couple of difficult cases are now analyzed. Fig. 8 shows a very low contrast between a noisy seafloor and a different texture region. As may be seen, the segmentation approach with ACA–CFAR 2-D performs well, as in Fig. 9, where a noisy image of a pipeline is presented. The experiment settings are given in Table III.

Fig. 10 shows the comparison with the techniques presented in [1]. Results of this set of experiments are summed up in Table IV, while the experiment settings are given in Table V.

The algorithm proposed in this paper drastically improves computation times for close similar segmentation results, which

was one of the original objectives of this work. Only with the setting of three parameters (the probability of false alarm, and the numbers of reference and guard cells), and without resorting to any complex model, a very good and useful segmentation can be obtained. This feature gives robustness to the approach. As discussed in [28], segmentation is very much application dependant and constitutes only the first step toward pattern recognition in a robotic perception system. Hence, the comparison to ground-truth segmentation approach is just a subjective comparison. For this reason, even when the results for ACA–CFAR 2-D represented by the performance index ρ in Table IV seem worse than the UDWT results, there are applications such as the determination of free-span or rock-dump grounds in pipeline inspections, for which a segmentation such as the one in Fig. 10(e) will be preferable. ACA–CFAR 2-D generates an appropriate level of useful detail for the computation of descriptors in pattern classification.

VI. Conclusion

This paper presented an algorithm capable of efficiently performing segmentation into two types of regions: acoustical highlight and seafloor reverberation areas from seafloor images obtained by an SSS. Its efficiency was not only measured by computational time but also supported by an algorithmic complexity measure. In addition, from this segmentation, a robust detection was achieved in the automated pipeline detection and tracking domain. The simplicity of the use of ACA–CFAR 2-D can be summarized as follows: 1) only three parameters need to be set before inspection; and 2) the algorithmic complexity is upper bounded to $O(N^2)$. These three mentioned parameters must be selected considering the device providing the acoustic data and the application to be faced.

The proposed ACA–CFAR 2-D algorithm represents a variation of a technique widely used in radar technology for detecting moving objects in real time. In this way, this paper provides a twofold demonstration. First, it demonstrates that adopting ideas from radar to sonar to make detections in real time is fruitful and inspiring. Second, as a segmentation technique, ACA–CFAR 2-D was compared to other commonly used techniques. It exhibited almost the same successful results with respect to active contours and UDWT, with much less computational resources and, thus, with faster responses. The comparative results with the UDWT segmentation technique, for instance, showed a decrease of approximately 85% in computational complexity, with a robust behavior against noise. However, this fact does not mean that one can replace one segmentation approach by the other in a general way. The final selection is highly domain dependent. For online tracking, ACA–CFAR 2-D exhibits a wonderful behavior. Besides, for offline cartography construction, UDWT based on a contextual model rather than on a pixel-by-pixel detection, is a better option. Further, ACA–CFAR 2-D may be used as a good preprocessing tool for UDWT in such case.

All of these features are of great interest to incorporate the ACA–CFAR 2-D algorithm in the perception system of an aquatic robot such as an AUV or an autonomous surface vehicle (ASV), which must make decisions in real time to provide feedback efficiently to a dynamic mission replanner or an adaptive control of the robot based on data acquired from sonar.

Acknowledgment

The authors would like to thank MSc. Eng. André Sousa for his great support in data collection in Brazil, and the anonymous reviewers for their valuable help and contribution in the final quality of this paper. S. A. Villar acknowledges the IEEE/OES Student Scholarships which he was granted for his postgraduate studies.

References

[1] T. Celik and T. Tjahjadi, "A novel method for sidescan sonar image segmentation," *IEEE J. Ocean. Eng.*, vol. 36, no. 2, pp. 186–194, Apr. 2011.

[2] A. Balasuriya and T. Ura, "Multi-sensor fusion for autonomous underwater cable tracking," in *Proc. MTS/IEEE OCEANS Conf.*, 1999, vol. 1, pp. 209–215.

[3] A. Balasuriya and T. Ura, "Vision-based underwater cable detection and following using AUVs," in *Proc. MTS/IEEE OCEANS Conf.*, 2002, vol. 3, pp. 1582–1587.

[4] M. Mignotte, C. Collet, and P. Bouthemy, "Markov random field and fuzzy logic modeling in sonar imagery: Application to the classification of underwater floor," *Comput. Vis. Image Understand.*, vol. 79, pp. 4–24, 2000.

[5] I. Ishøy *et al.*, "New challenges for AUTOTRACKER," presented at the Unmanned Underwater Vehicle Showcase, Southampton, U.K., 2002, unpublished.

[6] Y. R. Petillot, S. R. Reed, and J. M. Bell, "Real time AUV pipeline detection and tracking using side scan sonar and multi-beam echo-sounder," in *Proc. MTS/IEEE OCEANS Conf.*, 2002, vol. 1, pp. 217–222.

[7] X. Lurton, *An Introduction to Underwater Acoustics: Principles and Applications*. New York, NY, USA: Springer-Verlag, 2002, ch. II, III, and VIII.

[8] S. Reed, Y. R. Petillot, and J. Bell, "A model based approach to mine detection and classification in sidescan sonar," in *Proc. OCEANS Conf.*, 2003, vol. 3, pp. 1402–1407.

[9] S. Reed, I. Tena Ruiz, C. Capus, and Y. R. Petillot, "The fusion of large scale classified side-scan sonar image mosaics," *IEEE Trans. Image Process.*, vol. 15, no. 7, pp. 2049–2060, Jul. 2006.

[10] P. Brehmer *et al.*, "New applications of hydroacoustic methods for monitoring shallow water aquatic ecosystems: The case of mussel culture grounds," *Aquat. Living Resour.*, vol. 16, no. 3, pp. 333–338, 2003.

[11] L. Hellequin, J.-M. Boucher, and X. Lurton, "Processing of high-frequency multibeam echo sounder data for seafloor characterization," *IEEE J. Ocean. Eng.*, vol. 28, no. 1, pp. 78–89, Jan. 2003.

[12] S. Reed, Y. R. Petillot, and J. Bell, "Automated approach to classification of mine-like objects in sidescan sonar using highlight and shadow information," *Inst. Electr. Eng. Proc.—Radar Sonar Navig.*, vol. 151, no. 1, pp. 48–56, Feb. 2004.

[13] S. W. Perry and L. Guan, "A recurrent neural network for detecting objects in sequences of sector-scan sonar images," *IEEE J. Ocean. Eng.*, vol. 29, no. 3, pp. 857–871, Jul. 2004.

[14] G. L. Chenadec and J.-M. Boucher, "Sonar image segmentation using the angular dependence of backscattering distributions," in *Proc. OCEANS Eur. Conf.*, 2005, vol. 1, pp. 147–152.

[15] J. Bell *et al.*, "Adaptive fusion architecture for context aware detection and classification," in *Proc. OCEANS Eur. Conf.*, 2007, DOI: 10.1109/OCEANSE.2007.4302247.

[16] R. E. Hansen, H. J. Callow, T. O. Saebo, P. E. Hagen, and B. Langli, "High fidelity synthetic aperture sonar products for target analysis," in *Proc. OCEANS Conf.*, 2008, DOI: 10.1109/OCEANS.2008.5152071.

[17] P. Chapple, "Automated detection and classification in high-resolution sonar imagery for autonomous underwater vehicle operations," Austral. Defence Sci. Technol. Organisation, Rep. DSTO-GD-0537, Dec. 2008.

[18] P. B. Chapple, "Unsupervised detection of mine-like objects in seabed imagery from autonomous underwater vehicles," in *Proc. MTS/IEEE OCEANS Conf.*, 2009.

[19] T. O. Saebo, H. J. Callow, R. E. Hansen, B. Langli, and E. O. Hammerstad, "Bathymetric capabilities of the HISAS interferometric synthetic aperture sonar," in *Proc. OCEANS Conf.*, 2007, DOI: 10.1109/OCEANS.2007.4449357.
[20] P. E. Hagen and R. E. Hansen, "Synthetic aperture sonar on AUV: Making the right trade-offs," *J. Ocean Technol.*, vol. 6, no. 2, pp. 17–22, 2011.
[21] D. P. Williams, "Bayesian data fusion of multiview synthetic aperture sonar imagery for seabed classification," *IEEE Trans. Image Process.*, vol. 18, no. 6, pp. 1239–1254, Jun. 2009.
[22] A. M. Pavin, "The pipeline identification method basing on AUV's echo-sounder data," in *Proc. OCEANS Conf.*, 2006, DOI: 10.1109/OCEANS.2006.306795.
[23] S. F. Greenaway and T. C. Weber, "Test methodology for evaluation of linearity of multibeam echosounder backscatter performance," in *Proc. OCEANS Conf.*, 2010, DOI: 10.1109/OCEANS.2010.5664383.
[24] M. Lianantonakis and Y. R. Petillot, "Sidescan sonar segmentation using texture descriptors and active contours," *IEEE J. Ocean. Eng.*, vol. 32, no. 3, pp. 744–752, Jul. 2007.
[25] X.-F. Ye, Z.-H. Zhang, P. X. Liu, and H.-L. Guan, "Sonar image segmentation based on GMRF and level-set models," *Ocean Eng.*, vol. 37, no. 10, pp. 891–901, 2010.
[26] M. Mignotte, C. Collet, P. Pérez, and P. Bouthemy, "Three-class Markovian segmentation of high-resolution sonar images," *Comput. Vis. Image Understand.*, vol. 76, no. 3, pp. 191–204, 1999.
[27] S. A. Villar, G. G. Acosta, A. L. Sousa, and A. Rozenfeld, "Evaluation of an efficient approach for target tracking from acoustic imagery for the perception system of an autonomous underwater vehicle," *Int. J. Adv. Robot. Syst.*, vol. 11, no. 24, 2014, DOI: 10.5772/56954.
[28] R. C. Gonzalez and R. E. Woods, *Digital Image Processing*, 2nd ed. Upper Saddle River, NJ, USA: Prentice-Hall, 2001, ch. II and X.
[29] F. Schmitt, M. Mignotte, C. Collet, and P. Thourel, "Estimation of noise parameters on sonar images," *SPIE Signal Image Process.*, vol. 2823, pp. 1–12, 1996.
[30] C. Collet, P. Thourel, P. Perez, and P. Bouthemy, "Hierarchical MRF modeling for sonar picture segmentation," in *Proc. Int. Conf. Image Process.*, 1996, vol. 3, pp. 979–982.
[31] W. K. Pratt, *Digital Image Processing: PIKS Inside*, 3rd ed. New York, NY, USA: Wiley, 2001, ch. II and V.
[32] B. Zerr, E. Maillard, and D. Gueriot, "Sea-floor classification by neural hybrid system," in *Proc. OCEANS Conf.*, 1994, vol. 2, pp. 239–243.
[33] D. R. Carmichael, L. M. Linnett, S. J. Clarke, and B. R. Calder, "Seabed classification through multifractal analysis of sidescan sonar imagery," *Inst. Electr. Eng. Proc.—Radar Sonar Navig.*, vol. 143, no. 3, Jun. 1996, DOI: 10.1049/ip-rsn:19960472.
[34] I. Karoui, R. Fablet, J.-M. Boucher, and J.-M. Augustin, "Seabed segmentation using optimized statistics of sonar textures," *IEEE Trans. Geosci. Remote Sens.*, vol. 47, no. 6, pp. 1621–1631, Jun. 2009.
[35] G. Cutter, Y. Rzhanov, and L. Mayer, "Automated segmentation of seafloor bathymetry from multibeam echosounder data using local Fourier histogram texture features," *J. Exp. Mar. Biol. Ecol.*, vol. 285–286, pp. 355–370, 2003.
[36] T. F. Chan, B. Y. Sandberg, and L. A. Vese, "Active contours without edges for vector-valued images," *J. Vis. Commun. Image Represent.*, vol. 11, no. 2, pp. 130–141, 2000.
[37] J.-L. Starck, J. Fadili, and F. Murtagh, "The undecimated wavelet decomposition and its reconstruction," *IEEE Trans. Image Process.*, vol. 16, no. 2, pp. 297–309, Feb. 2007.
[38] D. K. Barton and S. A. Leonov, *Radar Technology Encyclopedia*. Reading, MA, USA: Artech House, 1998, pp. 91–93.
[39] M. A. Richards, *Fundamental of Radar Signal Processing*. New York, NY, USA: McGraw-Hill, 2005, ch. VI and VII.
[40] S. M. Kay, *Fundamentals of Statistical Signal Processing. Estimation Theory*. Upper Saddle River, NJ: Prentice-Hall, 1993, ch. VII.
[41] M. I. Skolnik, *Radar Handbook*, 2nd ed. New York, NY, USA: McGraw-Hill, 1990.
[42] V. K. Rohatgi and M. D. E. Saleh, *An Introduction to Probability and Statistics*, 2nd ed. New York, NY, USA: Wiley, 2011, ch. II.
[43] S. A. Villar, A. L. Sousa, A. Rozenfeld, and G. G. Acosta, "Pipeline detection system in acoustic images utilizing CA-CFAR," in *Proc. MTS/IEEE OCEANS Conf.*, 2013.
[44] C. J. Venter, H. Grobler, and K. A. AlMalki, "Implementation of the CA-CFAR Algorithm for pulse-Doppler Radar on a GPU Architecture," in *Proc. IEEE Conf. Appl. Electr. Eng. Comput. Technol.*, Amman, Jordan, 2011, DOI: 10.1109/AEECT.2011.6132514.
[45] P. Viola and M. Jones, "Rapid object detection using a boosted cascade of simple features," in *Proc. IEEE Comput. Soc. Conf. Comput. Vis. Pattern Recognit.*, 2001, vol. 1, pp. I-511–I-518.
[46] G. Bradski and A. Kaehler, *Learning OpenCV: Computer Vision With the OpenCV Library*, 1st ed. New York, NY, USA: O'Reilly Media, 2008, ch. III, IV, and IX.
[47] EdgeTech [Online]. Available: http://www.edgetech.com/
[48] Marine Sonic Technology, Ltd. [Online]. Available: http://www.marinesonic.us/

Gerardo G. Acosta (SM'01) graduated as Engineer in electronics from the National University of La Plata, La Plata, Buenos Aires, Argentina, in 1988, and received the Ph.D. degree in computer science from the University of Valladolid, Valladolid, Spain, in 1995.

He is currently a Full Professor in Control Systems at the Engineering Faculty, National Buenos Aires Province Centre University (UNCPBA), Olavarría, Argentina. He is also a researcher of the Argentinean National Research Council (CONICET), and Head of the R&D Group "INTELYMEC," at the Engineering Faculty, UNCPBA. His working interests comprise intelligent control and image processing in terrestrial and underwater robotics. He has more than 120 publications and two copyrights in this and related fields. He has been awarded with the INNOVAR 2011 second position in robotics, for the autonomous robot CARPINCHO, and with the INNOVAR 2012 first position in robotics, for the autonomous underwater vehicle ICTIOBOT, both developed at INTELYMEC. He has been a research leader of more than ten R&D projects, funded by the Argentinean Government, the Spanish Government, and the European Union. He has been invited as a professor of Ph.D. programs in Argentina and Spain. He is the present Director of the Ph.D. program at the Engineering Faculty, UNCPBA.

Prof. Acosta was Chairman of the IEEE Computational Intelligence Society (CIS) Argentinean Chapter (2007–2008), receiving the 2010 Outstanding Chapter Award from CIS, and current Chairman of the IEEE Oceanic Engineering Society Argentinean Chapter, being one of its founders. He serves as reviewer and member of scientific committees of several national and international journals and conferences.

Sebastián A. Villar (M'10) graduated as a Systems Engineer from the Faculty of Exact Sciences, National Buenos Aires Province Centre University (UNCPBA), Olavarría, Argentina, in 2009 and received the MBA degree from the Faculty of Economic Science, UNCPBA, in 2011. He is currently working toward the Ph.D. degree in engineering at INTELYMEC Group, Engineering Faculty, UNCPBA, with a scholarship from CONICET and IEEE Oceanic Engineering Society Student grant.

He is an Assistant Lecturer of Computer Sciences at the Engineering Faculty, UNCPBA. His working topics involve acoustic image processing for robotics and oceanographic applications.